# THE SLOWLY PULSATING B-STAR 18 PEG:
# A TESTBED FOR UPPER MAIN SEQUENCE STELLAR EVOLUTION

A. Irrgang[1], P. De Cat[2], A. Pigulski[3], G. Handler[4], A. Tkachenko[5] and the BRITE team

**Abstract.** The predicted width of the upper main sequence in stellar evolution models depends on the empirical calibration of the convective overshooting parameter. Despite decades of discussions, its precise value is still unknown and further observational constraints are required to gauge it. In 2016, Irrgang et al. discovered that the mid B-type subgiant 18 Peg is one of the most evolved members of the rare class of slowly pulsating B-stars and, thus, bears some potential to derive a tight lower limit for the width of the upper main sequence. Here we report on new photometric and spectroscopic analyses based on follow-up observations obtained with the BRITE-Heweliusz satellite and the Hermes spectrograph, which, among others, led to a revised oscillation frequency as well as to an updated radial-velocity curve of this single-lined spectroscopic binary system.

Keywords: binaries: spectroscopic, stars: early-type, stars: individual: 18 Peg, stars: oscillations

## 1 Introduction

The phenomenon of slowly pulsating B (SPB) stars is more or less restricted to the main-sequence (MS) phase due to the very strong damping of high-order gravity modes in the interiors of post-MS stars (e.g., Pamyatnykh 1999; Moravveji 2016). The most-evolved SPB stars may thus be used to derive a lower limit on the width of the upper MS, which is an important constraint for stellar evolution models. Irrgang et al. (2016) showed that the program star 18 Peg is one of those very evolved SPB stars that bear such a potential. Triggered by this finding, we have collected follow-up observations with the BRITE-Heweliusz satellite and the Hermes spectrograph to study 18 Peg's properties in further detail.

## 2 Analyses

For the analysis of the new data, we followed almost exactly the methods applied by Irrgang et al. (2016), which is why we refer the interested reader to that paper for details about the analysis and just focus on the new results here. Please note that all uncertainties given in this work are $1\sigma$.

### 2.1 Analyses of the light curves

The investigation of the photometric variability of 18 Peg is based on data from the BRITE-Heweliusz satellite (almost continuously observing it for 140 days) as well as on differential Strömgren $u$ and $y$ magnitudes taken with the Automatic Photoelectric Telescope (APT) T6 at Fairborn Observatory in Arizona (471 measurements spread over 90 days). Those data sets constitute a significant improvement over the scarcely sampled Tycho and Hipparcos epoch photometry which was used by Irrgang et al. (2016) and which allowed to find a single oscillation frequency of $\sim 0.72\,\mathrm{d}^{-1}$. The new results are illustrated in Figs. 1 and 2 and summarized in Table 1. Owing to the excellent temporal coverage of the BRITE light curve, it is now obvious that the signal at $\sim 0.72\,\mathrm{d}^{-1}$ is actually just a daily alias of the true frequency at $0.28876 \pm 0.00012\,\mathrm{d}^{-1}$, which, like the other detected frequencies at $0.4541 \pm 0.0004\,\mathrm{d}^{-1}$ and $0.1660 \pm 0.0005\,\mathrm{d}^{-1}$, is compatible with an SPB nature of 18 Peg.

[1] Dr. Karl Remeis-Observatory Bamberg & ECAP, Sternwartstr. 7, 96049 Bamberg, Germany (e-mail: andreas.irrgang@fau.de)

[2] Royal Observatory of Belgium, Ringlaan 3, B-1180 Brussels, Belgium

[3] Wroclaw University, Astronomical Institute, Kopernika 11, 51-622 Wroclaw, Poland

[4] Copernicus Astronomical Center, Bartycka 18, 00-716 Warszawa, Poland

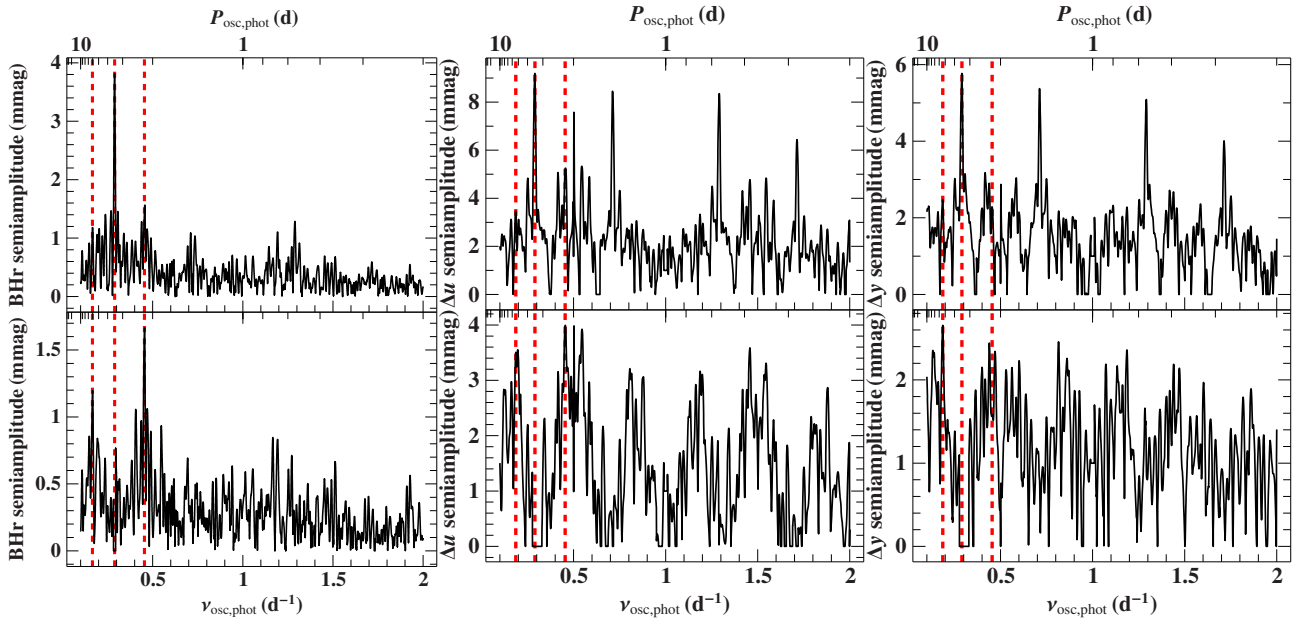[5] Instituut voor Sterrenkunde, KU Leuven, Celestijnenlaan 200D, B-3001 Leuven, Belgium

**Fig. 1.** The frequency spectra derived from photometric data taken with the BRITE-Heweliusz satellite (*left column*) as well as from differential Strömgren $u$ (*middle column*) and $y$ (*right column*) data taken with APT. The curves in the *upper row* are based on the original data while those in the *lower row* have been prewhitened by $\nu_{\rm osc} \sim 0.29\,{\rm d}^{-1}$, i.e., the frequency exhibiting the strongest strong signal in the original data. The ground-based data show additional signals from daily aliases of this frequency. The red dashed, vertical lines mark the three detected signals.
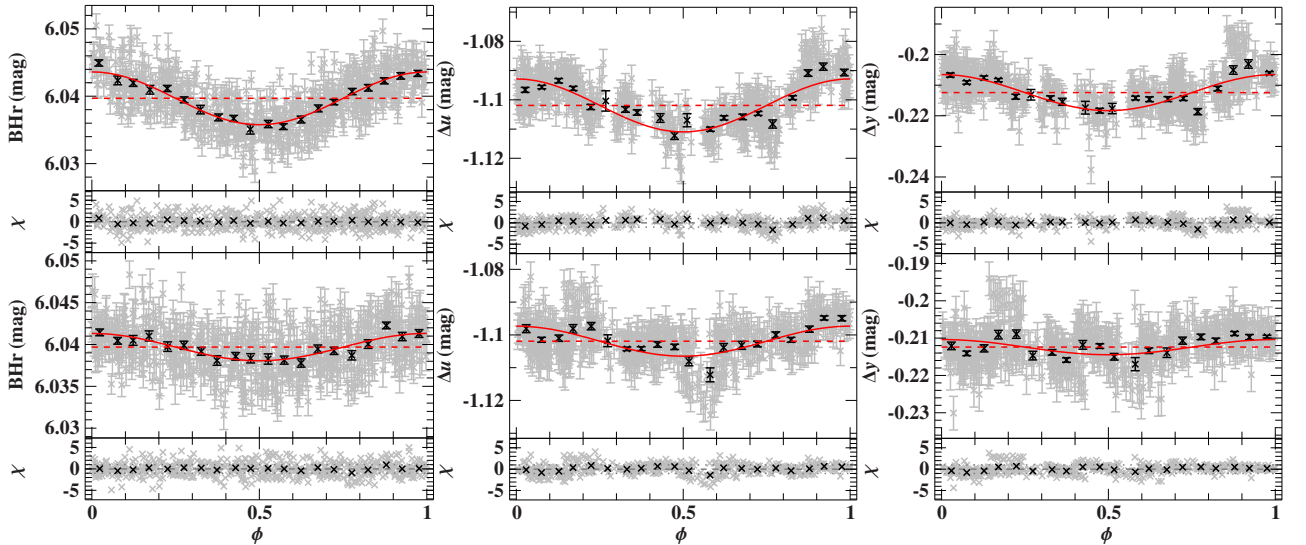


**Fig. 2.** Phased and prewhitened light-curves of BRITE-Heweliusz (*left column*) and differential Strömgren $u$ (*middle column*) and $y$ (*right column*) data for the first (*upper row*) and second (*lower row*) detected mode ($\phi = 0$ corresponds to the maximum brightness within the pulsation cycle): the measurements are represented by gray crosses with error bars (BRITE-Heweliusz data are orbital averages) while the best-fitting model (see Table 1) is indicated by the red solid curve. The red dashed line marks the derived mean magnitude. The black points are phase-averaged values that were just added to guide the eye. Residuals $\chi$, i.e., the difference between observation and model divided by the respective uncertainty, are shown as well.

### 2.2 Analysis of the spectral energy distribution and of the spectra

Owing to the availability of improved spectral models (Irrgang et al. 2018) and new data, e.g., taken with the HERMES spectrograph, we repeated the analysis of the spectral energy distribution (Fig. 3) and the spectroscopic analysis (Fig. 4). The resulting atmospheric parameters are listed in Table 2 and are now much more consistent with each other and still compatible with an SPB star.

**Table 1.** Results of the light-curve analysis.

| Parameter | Mode 1 | Mode 2 | Mode 3 |
|---|---|---|---|
| BRITE-Heweliusz data: | | | |
| Period $P_{\rm osc}$ (d) | $3.4630^{+0.0015}_{-0.0014}$ | $2.2020^{+0.0018}_{-0.0017}$ | $6.023^{+0.017}_{-0.015}$ |
| Frequency $\nu_{\rm osc}$ (d$^{-1}$) | $0.28876 \pm 0.00012$ | $0.4541 \pm 0.0004$ | $0.1660 \pm 0.0005$ |
| Phase $\phi_{\rm ref}$ at epoch $T_{\rm ref}$ | $0.697^{+0.010}_{-0.009}$ | $0.707^{+0.028}_{-0.026}$ | $0.501^{+0.032}_{-0.029}$ |
| BHr semiamplitude (mmag) | $3.92 \pm 0.11$ | $1.63 \pm 0.10$ | $1.17 \pm 0.10$ |
| BHr mean magnitude (mag) | $6.03969^{+0.00007}_{-0.00008}$ | | |
| Differential Strömgren data: | | | |
| Period $P_{\rm osc}$ (d) | $3.4470^{+0.0023}_{-0.0030}$ | $2.2007^{+0.0013}_{-0.0023}$ | $5.373^{+0.007}_{-0.011}$ |
| Frequency $\nu_{\rm osc}$ (d$^{-1}$) | $0.29010^{+0.00025}_{-0.00020}$ | $0.45440^{+0.00048}_{-0.00025}$ | $0.18612^{+0.00038}_{-0.00022}$ |
| Phase $\phi_{\rm ref}$ at epoch $T_{\rm ref}$ | $0.13^{+0.07}_{-0.05}$ | $0.61^{+0.15}_{-0.09}$ | $0.915^{+0.028}_{-0.017}$ |
| $\Delta u$ semiamplitude (mmag) | $9.05^{+0.34}_{-0.30}$ | $4.57^{+0.31}_{-0.27}$ | $4.18^{+0.35}_{-0.26}$ |
| $\Delta y$ semiamplitude (mmag) | $5.9 \pm 0.4$ | $2.03^{+0.30}_{-0.28}$ | $3.00^{+0.33}_{-0.30}$ |
| $\Delta u$ mean magnitude (mag) | $-1.10191^{+0.00021}_{-0.00026}$ | | |
| $\Delta y$ mean magnitude (mag) | $-0.21242^{+0.00021}_{-0.00025}$ | | |
| Fixed reference epoch $T_{\rm ref}$ (HJD$-2\,400\,000.5$) | $57\,939.0$ | | |
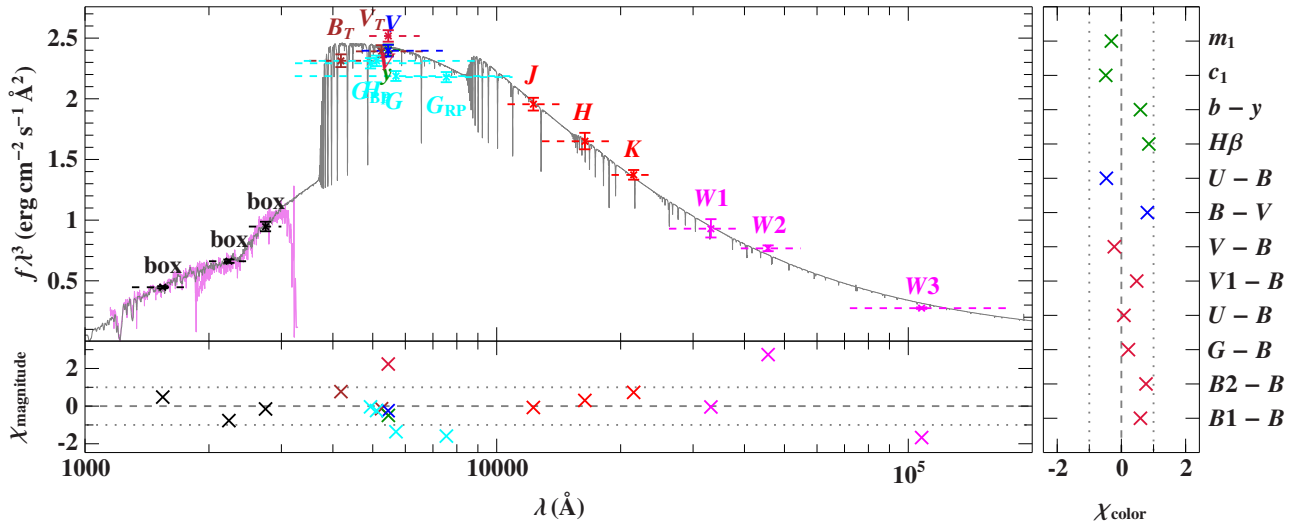


**Fig. 3.** Comparison of synthetic and observed photometry: The *top panel* shows the spectral energy distribution. The colored data points are filter-averaged fluxes which were converted from observed magnitudes (the respective filter widths are indicated by the dashed horizontal lines), while the gray solid line represents the best-fitting model (see Table 2) degraded to a spectral resolution of 6 Å. The three black data points labeled "box" are fluxes converted from magnitudes computed by means of box filters of the indicated width from IUE spectra (magenta line). The panels at the *bottom* and on the *side* show the residuals for magnitudes and colors, respectively. The photometric systems have the following color code: Tycho (brown); *Gaia* and HIPPARCOS (cyan); Johnson-Cousins (blue); Strömgren (green); Geneva (crimson); 2MASS (red); WISE (magenta).

**Table 2.** Stellar parameters derived from photometry and spectroscopy.

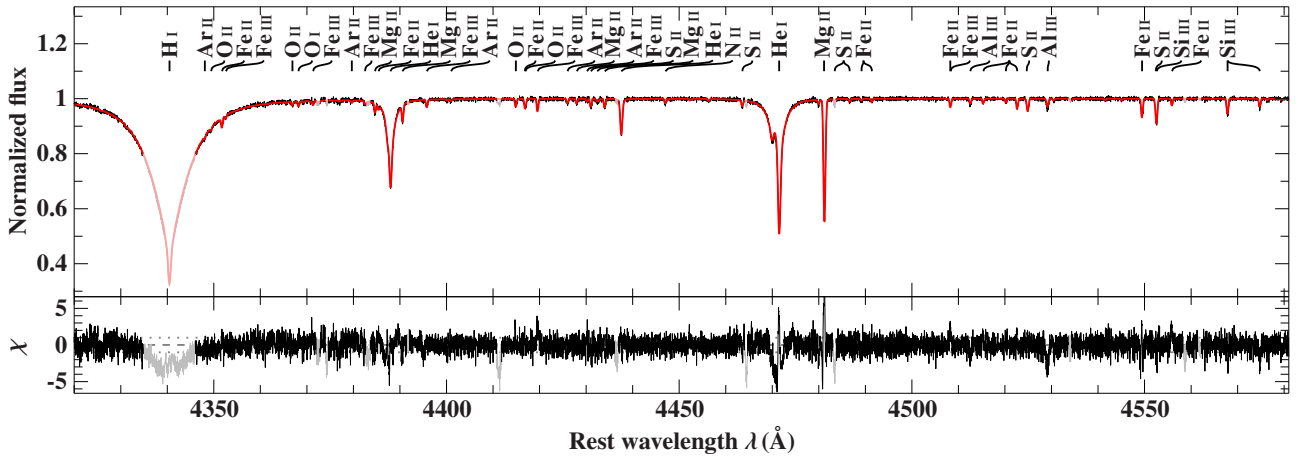| Parameter | Photometry | Spectrocopy |
|---|---|---|
| Angular diameter $\log(\Theta\,({\rm rad}))$ | $-9.1495 \pm 0.0025$ | ... |
| Color excess $E(B-V)$ | $0.055 \pm 0.006\,{\rm mag}$ | ... |
| Extinction parameter $R_V$ (fixed) | $3.1$ | ... |
| Effective temperature $T_{\rm eff}$ | $15\,080^{+170}_{-160}\,{\rm K}$ | $15\,260 \pm 160\,{\rm K}$ |
| Surface gravity $\log(g\,({\rm cm\,s^{-2}}))$ | $3.72 \pm 0.16$ | $3.59 \pm 0.04$ |

**Fig. 4.** Exemplary comparison of the best-fitting model spectrum (red line, see Table 2) with one of the re-normalized HERMES spectra (black line). Light colors mark regions that have been excluded from fitting. Residuals $\chi$ are shown as well.

### 2.3 Analysis of the line-profile variations

To study the pulsationally induced temporal distortions of the spectral line profiles, we fitted nine different spectral lines in 59 epochs using a purely dynamical model for the velocity field of an adiabatically pulsating star whose pulsational and rotational axes are aligned (Schrijvers et al. 1997). Two oscillation modes were included in the model. While the observed frequency (for a definition see Ledoux 1951) of the first mode was restricted to a small interval around the result of the light-curve analysis, we left the second one as a free parameter to allow for modes that are only visible in the line-profile variations, e.g., because of cancellation effects of modes with high degree $l$ or azimuthal order $m$ in the light curve. Figure 5 shows an exemplary comparison between observations and best-fitting model. Despite the additional mode, the model is not able to decently reproduce the observations for all epochs, which may be a consequence of all the simplifying assumptions made in the model. Consequently, the parameters of the best-fitting model, which are listed in Table 3 and whose meaning is described in Irrgang et al. (2016), are currently not reliable and a more sophisticated treatment of the line-profile variations is needed.
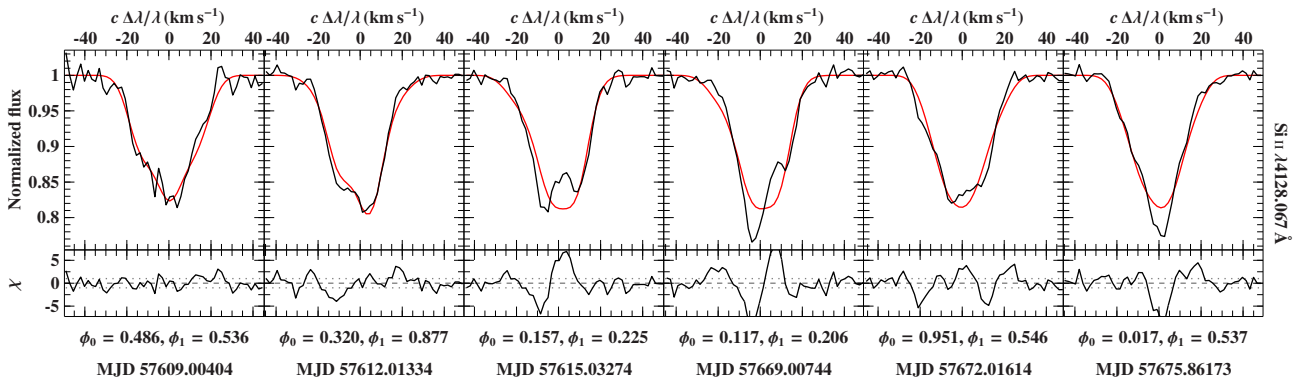


**Fig. 5.** Spectral modeling of the pulsationally driven line-profile distortions for six exemplary epochs (*columns*) and one exemplary spectral line: the HERMES observations are indicated by a black line, the model (see Table 3) by a red one, and the quality of the fit by the residuals $\chi$. Observed oscillation phases for both modes are listed on the x-axes.

### 2.4 Analysis of the radial-velocity curve

The updated model for the spectral line-profile variations as well as the new HERMES observations allow us to revise the radial-velocity curve of this single-lined spectroscopic binary system. In contrast to Irrgang et al. (2016), we solely rely here on high-resolution spectra to extract radial velocities. Figure 6 shows the new solution

**Table 3.** Parameters of the best-fitting model for the line-profile variations.

| Most relevant parameters affecting (the) | | | | | | | | | | | | Derived quantities from (the) | | | | | | | | | | |
| --- | --- | --- | --- | --- | --- | --- | --- | --- | --- | --- | --- | --- | --- | --- | --- | --- | --- | --- | --- | --- | --- | --- |
| first mode | | | | | | second mode | | | | both modes | | first mode | | second mode | | | | both modes | | | | |
| $l$ | $m$ | $\langle v_v^2 \rangle^{1/2}$ | $k^{(0)}$ | $\frac{\nu_{\rm rot}}{\nu_{\rm osc}^{(0)}}$ | $\nu_{\rm osc}^{\rm obs}$ | $l$ | $m$ | $\langle v_v^2 \rangle^{1/2}$ | $\nu_{\rm osc}^{\rm obs}$ | $i$ | $v\sin(i)$ | $a_{\rm sph}$ | $\nu_{\rm osc}^{(0)}$ | $k^{(0)}$ | $\frac{\nu_{\rm rot}}{\nu_{\rm osc}^{(0)}}$ | $a_{\rm sph}$ | $\nu_{\rm osc}^{(0)}$ | $\eta$ | $\nu_{\rm rot}$ | $M$ | $R_\star$ | $\log(g)$ |
| | | km s$^{-1}$ | | | d$^{-1}$ | | | km s$^{-1}$ | d$^{-1}$ | ° | km s$^{-1}$ | $R_\odot$ | d$^{-1}$ | | | $R_\odot$ | d$^{-1}$ | d$^{-1}$ | | $M_\odot$ | $R_\odot$ | cgs |
| 2 | +2 | 0.569 | 2.46 | 0.205 | 0.277 | 4 | −4 | 0.798 | 0.778 | 24.5 | 19.68 | 0.12 | 0.444 | 2.71 | 0.215 | 0.19 | 0.423 | 0.02 | 0.091 | 7.2 | 10.3 | 3.27 |

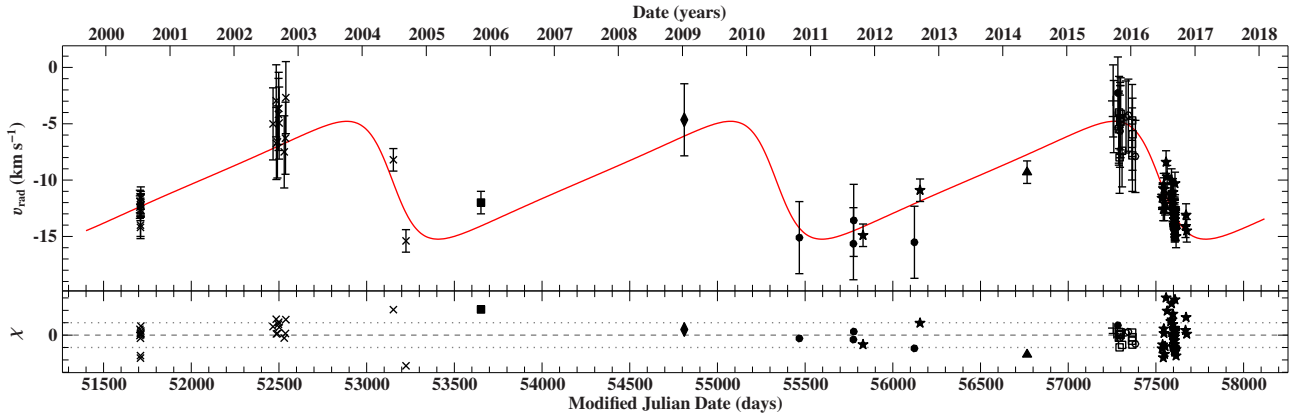whose parameters are listed in Table 4.



**Fig. 6.** Updated radial velocity curve of 18 Peg: the measurements are represented by black symbols with error bars while the best-fitting Keplerian model (see Table 4) is indicated by the red solid curve. Residuals $\chi$ are shown in the *lower panel*. The symbols identify different instruments, all of which are high-resolution spectrographs.

**Table 4.** Orbital parameters of the single-lined spectroscopic binary system.

| Parameter | Value |
| --- | --- |
| Period $P$ | $2188 \pm 10$ d |
| Epoch of periastron $T_{\rm periastron}$ | $57\,520 \pm 40$ MJD |
| Eccentricity $e$ | $0.42^{+0.06}_{-0.05}$ |
| Longitude of periastron $\omega$ | $90^{+10\circ}_{-\ 9}$ |
| Velocity semiamplitude $K_1$ | $5.2 \pm 0.4$ km s$^{-1}$ |
| Systemic velocity $\gamma$ | $-10.02^{+0.28}_{-0.27}$ km s$^{-1}$ |
| Derived parameter | Value |
| Mass function $f(M)$ | $0.024^{+0.007}_{-0.006}\,M_\odot$ |
| Projected semimajor axis $a_1\sin(i)$ | $0.95^{+0.09}_{-0.08}$ AU |
| Projected periastron distance $r_{\rm p}\sin(i)$ | $118^{+19}_{-18}\,R_\odot$ |

## 3 Discussion

Our revised atmospheric parameters still indicate that 18 Peg is one of the most evolved SPB stars known to date. However, as demonstrated in Fig. 7, its surface gravity does not seem to be low enough to put significant new constraints on current stellar models for the upper MS given that the results from line-profile fitting are unreliable because they are based on a model that is probably too simplistic.
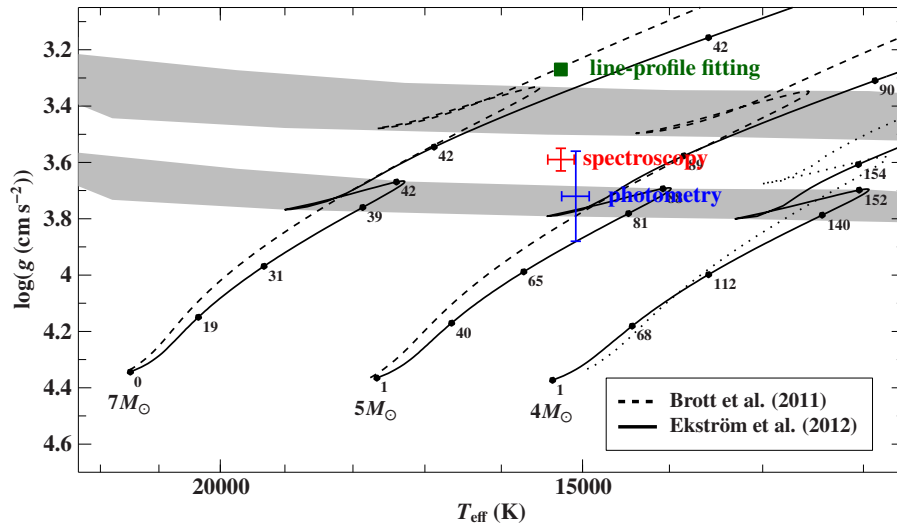
**Fig. 7.** Position of 18 Peg in a ($T_\text{eff}$, $\log(g)$) diagram based on spectroscopy, photometry, and fitting of the spectral line-profile variations ($T_\text{eff}$ taken from spectroscopy). Overlaid are evolutionary tracks for non-rotating stars of solar metallicity and different initial masses by Brott et al. (2011, dashed lines) and Ekström et al. (2012, solid lines). The gray-shaded areas highlight the transition region between MS and post MS for the two different sets of models, which primarily differ in the efficiency of convective overshooting. The impact of stellar rotation is demonstrated via the dotted line, which is an Ekström et al. (2012) track for a rotating ($\Omega/\Omega_\text{crit} = 0.4$) star with an initial mass of $4\,M_\odot$.

## References

Brott, I., de Mink, S. E., Cantiello, M., et al. 2011, A&A, 530, A115

Ekström, S., Georgy, C., Eggenberger, P., et al. 2012, A&A, 537, A146

Irrgang, A., Desphande, A., Moehler, S., Mugrauer, M., & Janousch, D. 2016, A&A, 591, L6

Irrgang, A., Kreuzer, S., Heber, U., & Brown, W. 2018, A&A, 615, L5

Ledoux, P. 1951, ApJ, 114, 373

Moravveji, E. 2016, MNRAS, 455, L67

Pamyatnykh, A. A. 1999, Acta Astron., 49, 119

Schrijvers, C., Telting, J. H., Aerts, C., Ruymaekers, E., & Henrichs, H. F. 1997, A&AS, 121, 343